Molecular Medicine

RESEARCH

Open Access

Glucagon secretion by pancreatic alpha-cells requires an intact tubulin-cytoskeleton-primary cilium axis

Elena Casanueva-Álvarez[1†], Alba Sanz-González[1†], Alicia Vilas[1], Patricia Cámara-Torres[1,2], Magalie A. Ravier[3], Sara Eslava-Alcon[4,5], M. Carmen Duran-Ruiz[4,5], Cristina M. Ramírez[6], Peristera-Ioanna Petropoulou[7,8], Teresa Rodriguez-Calvo[7,8], Beatriz Merino[1,2,9], Germán Perdomo[1,2] and Irene Cozar-Castellano[1,2,10*]

Abstract

Background Hyperglucagonemia is a hallmark of diabetes mellitus, resulting from the dysregulation of glucagon secretion by pancreatic alpha-cells. Although glucose sensing and insulin signaling are well-established regulatory processes, the pathways that govern glucagon secretion remain unclear. Recent evidences suggest that insulin-degrading enzyme (IDE) regulates glucagon secretion via an unknown pathway.

Methods Using IDE-immunoprecipitation proteomic data as a basis, we aimed to ascertain the molecular mechanisms downstream of IDE in the alpha-TC cell model. Knock-down studies of relevant genes involved in the functional pathways identified in the proteomic study, and its impact on glucagon secretion were performed. Primary cilium was stained and detected using confocal and STORM microscopies in alpha-TC cells and mouse pancreas.

Results Based on proteomic studies we focus our efforts on the relationship between IDE, tubulin cytoskeleton, and the primary cilium. Although IDE was not localized to the primary cilium of alpha-cells using confocal microscopy and STORM, its absence resulted in impaired ciliogenesis. Consistent with lower protein levels of the insulin receptor, the counterregulatory effect of insulin on glucagon secretion was reduced in IDE-deficient alpha-cells. Two cellular models of ciliary dysfunction (ARL13B-KD and IFT88-KD) resulted in impaired glucagon secretion, as well as a failure of insulin to suppress glucagon secretion in alpha-cells. Importantly, IDE, tubulin, ciliary markers (AcTubulin, ARL13B) and insulin receptor levels were diminished in glucose conditions of physiological glucagon repression.

Conclusions IDE acts as a mechanistic link between glucose levels, tubulin, and the primary cilium, regulating glucagon secretion in alpha-cells. The dysregulation of the tubulin-primary cilium axis induces glucagon secretion impairment.

Keywords Diabetes mellitus, Endocrine pancreas, Pancreatic alpha-cell, Glucagon, Insulin-degrading enzyme, Tubulin, Primary cilium

†Elena Casanueva-Álvarez and Alba Sanz-González contributed equally to this work.

*Correspondence:
Irene Cozar-Castellano
irene.cozar@uva.es

Full list of author information is available at the end of the article

Background

Primary cilia are tubulin-based highly conserved structures across species that projects from the cell plasma membrane. Historically considered vestigial organelles, two decades ago were recognized as important signaling hubs for cellular development, differentiation and function. In human pancreatic islets, primary cilia have been reported in alpha- and beta-cells, whereas in rat and mouse islets have been observed in alpha-, beta-, delta-, and pancreatic polypeptide-cells (Cho and Hughes 2022; Pablos et al. 2022; Sanchez et al. 2023; Lee and Hughes 2023; Muller et al. 2024).

Human ciliopathies are inherited mutations in ciliary genes resulting in either abnormal formation or function of primary cilia in a wide group of disorders such as the Alström syndrome, Bardet-Biedl syndrome, autosomal dominant polycystic kidney disease and microcephalic osteodysplastic primordial dwarfism type II. These entities are associated with metabolic phenotypes including central obesity, impaired glucose tolerance, altered insulin secretion, insulin resistance, early-onset diabetes and type 2 diabetes (T2D) (Lee and Hughes 2023; Zaghloul and Katsanis 2009; Girard and Petrovsky 2011; Iliuta et al. 2022).

The role of primary cilia in pancreas has been studied using knockout mouse models of genes involved in ciliogenesis or cilia function. Thus, a mutation in the gene that encodes the polaris protein, an intraflagelar transport protein (IFT88) required for cilia assembly, lead to the absence or shorter pancreatic cilia. The endocrine pancreas of *Ift88* knockout mice showed normal islets architecture except for increased beta-cells clustering, which was associated with impaired glucose tolerance in response to a glucose challenge (Volta et al. 2019). Tissue-specific deletion of *Ift88* in pancreatic beta-cells (βCKO mouse) not only affected intrinsic beta-cell functions (glucose sensing and insulin secretion), but also impaired glucose homeostasis, paracrine signals and abnormal circulating hormone levels leading to the development of diabetes without obesity (Volta et al. 2019; Hughes et al. 2020).

Insulin-degrading enzyme (IDE) is a multifunctional protein expressed in both human and mouse pancreatic islet cells, with the highest expression in alpha-cells. Our group has been studied this intriguing protein for several years and we have identified that IDE protein levels were decreased in beta-cells of T2D patients treated with oral hypoglycemic agents (Fernandez-Diaz et al. 2018). We have also studied the role of IDE on pancreatic insulin and glucagon secretion using tissue-specific knockout mouse models (B-IDE-KO and A-IDE-KO, respectively). Isolated islets from B-IDE-KO mice showed hallmarks of beta-cell immaturity, including constitutive insulin secretion (Fernandez-Diaz et al. 2019). Conversely, targeted deletion of IDE in alpha-cells (A-IDE-KO) triggered hyperglucagonemia and hyperinsulinemia. Hyperglucagonemia was attributable in part to dysregulation of glucagon secretion, more specifically, there was an impaired ability of IDE-deficient alpha-cells to suppress glucagon release in the presence of high glucose or insulin. Our observations in the A-IDE-KO study led us to hypothesize that impaired ciliogenesis may be related to glucagon dysregulation (Merino et al. 2022).

In this work, we sought to investigate the cellular and molecular mechanisms linking impaired ciliogenesis to dysregulated hormonal secretion by pancreatic alpha-cells, which maybe involved in diabetes pathogenesis.

Methods

A-IDE-KO mouse model

Mice were housed in ventilated cages under a 12:12-h light-dark cycle, fed regular chow diet and water ad libitum, at the animal facility of the University of Valladolid (UVa). Animals with homozygous (A-IDE-KO / *Gcg-Cre*^{ERT2}; *Ide*$^{f/f}$) or heterozygous (A-IDE-HT mice / *Gcg-Cre*^{ERT2}; *Ide*$^{f/+}$) loss of *Ide* expression in pancreatic alpha cells were generated and genotyped as previously described (Merino et al. 2022). The Animal Care and Use Committee of the UVa approved all experiments (protocol #8608731). All experiments were performed in accordance with EU guidelines and regulations. Authors complied with the ARRIVE guidelines.

Islet isolation

Mouse A-IDE-KO, A-IDE-HT and A-IDE-WT islets were isolated by pancreatic duct perfusion with collagenase V (1000 IU/mL; SIGMA) as previously described (Fernandez-Diaz et al. 2019).

AlphaTC1.9 culture, SiRNA and ShRNA experiments and glucagon secretion studies

AlphaTC1.9 cells (CRL-2350, ATCC, USA; derived from a pancreatic mouse adenoma) were cultured in Dulbecco's Modified Eagle's Medium (DMEM) supplemented with 16 mM glucose, 15 mM HEPES, 0.1 mM non-essential amino acids, 10% FBS, and 100 U/mL penicillin and 100 µg/mL streptomycin. For insulin signaling experiments, cells were serum-deprived overnight and then, incubated in the absence or the presence of 100 nM insulin at the indicated times.

ON-TARGET plus SMART pool siRNA targeting mouse IDE (IDE-KD), ARL13B (ARL13B-KD) or IFT88 (IFT88-KD) (Dharmacon) was transfected into alphaTC1.9 cells in the presence of Lipofectamine 2000 Transfection Reagent (Invitrogen) for 6 h. Cells were cultured for 48 h in cell medium before experimentation. ON-TARGET plus nontargeting pool was used as control

siRNA. To generate the αTC1.9-shRNA-IDE cell line and its control cells were transduced with a lentiviral vector containing IDE-shRNA or an empty vector. Afterwards, αTC1.9 cells were subjected to puromycin selection of stably infected cells. The vector used was pGreenPuro™ shRNA Cloning and Expression Lentivector (System Biosciences, USA).

For glucagon secretion studies, cells were first preincubated in 3 mM glucose for 2 h, and then, incubated first in 1 mM (Low) glucose secretion buffer for 30 min, and afterwards in 16 mM (High) glucose secretion buffer for 30 min. The extracellular medium was collected after each incubation, and glucagon concentration was measured by ELISA (Mercodia, Sweden). Glucagon secretion data were normalized in respect to the control condition in low glucose (Control_Low). We have measured DNA content of each cell well to normalize glucagon/DNA, afterwards, glucagon secretion in each condition is divided by the average glucagon level in Control_Low. In islets experiments insulin secretion was measured in the same extracellular medium by ultrasensitive insulin ELISA (Chrystalchem, USA).

Western blotting

Islets from A-IDE-KO mice and alphaTC1.9 cells were homogenized in lysis buffer (125 mM Tris pH 6.8, 2% SDS, and 1 mM DTT) supplemented with protease and phosphatase inhibitors and briefly sonicated. Afterwards, 20 μg of protein from the lysates were boiled 5 min in Laemmli Sample Buffer (LSB) (62.5 mM Tris-HCl pH 6.8, 5% glycerol, 1% SDS, 2.5% β-mercaptoethanol and 0.02% w/v bromophenol blue). Proteins were quantified using the Micro BCA Kit (Thermo Fisher Scientific), separated by SDS-PAGE, and then transferred to PVDF membranes (Millipore). Membranes were blocked for 1 h at room temperature using blocking buffer (PBS, 0.1% Tween-20, 5% w/v non-fat dry milk). Blots were incubated with the following antibodies: anti-Dync1h1 (1:10,000. #12345-1-AP, Proteintech), anti-IDE (1:40,000, #AB9210, Millipore); anti-insulin receptor β (1:2,000, #3025, Cell Signaling), anti-phospho-insulin receptor β (Tyr1150/1151) (1:2,000, #3024, Cell Signaling), anti-ARL13B (1:1,000, #75–287; Antibodies Inc), anti-IFT88 (1:10,000, #13967-1-AP; Proteintech), anti-acetylated-tubulin (1:10,000, #T6793; Millipore), anti-actin (1:40,000 #612656, BD Biosciences); anti-GAPDH (1:200,000, #MAB374, Millipore), anti-p84 (1:400,000, #ab487; Abcam), anti-Rabbit IgG-HRP (1:20,000, #711-035-152, Jackson Immunoresearch), anti-Mouse IgG-HRP (1:5,000, #NA9310V, Cytiva). Band intensity was quantified with the ImageJ software (NIH, Bethesda, MA, USA).

RT-qPCR

The following genes were checked for mRNA expression after 48 h of αTC1.9 cell transfection with siRNA-IDE, siRNA-ARL13B or siRNA-IFT88 (compared to siRNA-scramble): *Ide*, *Arl13b*, *Ift88*, *Insr*. RNA was extracted using Trizol (Invitrogen, USA), reverse transcription was performed with iScript cDNA Synthesis Kit (Biorad, USA) and qPCR was carried on with the following Taqman (Applied Biosystems, USA): *Dync1h1* (Mm00466548_m1), *Ide* (Mm00473077_m1), *Arl13b* (Mm01349328_m1), *Ift88* (Mm01313467_m1), *Insr* (Mm01211875_m1). Results were normalized by *L18* Taqman results (Metabion, Germany).

In all experiments performed with siRNAs, the experimental condition was compared to siRNA-scramble. To discard differences in genes expression in cells without siRNA, comparative RT-qPCR (of the main genes under study) were performed comparing no siRNA versus siRNA-scramble cells (Supplementary Fig. 1).

Immunoprecipitation

AlphaTC1.9 cells (70–80% confluence) were lysated in 500 μL of lysis buffer (50 mM Tris-HCl, 150 mM NaCl, 1% (v/v) NP-40 pH = 8) supplemented with protease and phosphatase cocktail inhibitors (Sigma, USA). Immunoprecipitations of lysates (3–4 μg/μL of protein) were carried out using Dynabeads Protein A Immunoprecipitation kit (#10006D, Invitrogen, USA) and polyclonal antibodies against IDE (#AB9210, Millipore, USA). Briefly, Dynabeads were resuspended and washed in 200 μL of the Binding and Washing buffer following manufacturer's instruction. IDE antibody was incubated overnight with the cell lysates to form antibody-antigen complexes. The complexes were then captured by adding Dynabeads to the sample (2 h at 4 °C), followed by magnetic separation. The immunocomplexes captured on the Dynabeads were washed with Washing buffer, and eluted in 20 μL Elution buffer following manufacturer's instruction. Eluted samples were frozen at -80 °C for further proteomic analyses.

Proteomic analysis

Protein samples were incubated with 100 μL of lysis buffer containing 1% SDS, 5 mM Tris (2-carboxyethyl) phosphine, 10 mM chloroacetamide, 100 mM Tris (pH 8,5), and protease inhibitors (Roche cOmplete™ Mini, EDTA free Protease Inhibitor Cocktail). Samples were denatured, reduced and alkylated during 10 min at 95 °C and 1400 rpm. The entire lysate volume was retained for downstream processing in order to ensure comprehensive protein recovery from the full sample. Protein digestion was carried out using the MagReSyn Hydroxyl magnetic beads (ReSyn Biosciences, Edenvale, Gauteng, South Africa), following the PAC protocol, as described

(Rojas-Torres et al. 2024), with some modifications. Initially, 100% acetonitrile was added to reach a final concentration of 70% (v/v) acetonitrile in the lysate, followed by the addition of 10 µL of magnetic beads. Samples were incubated under agitation at room temperature for two cycles of 10 min. Bead-bound proteins were then washed in two sequential steps: two washes with 95% acetonitrile and two washes with 70% ethanol, each for 5 min. After the washing steps, proteins were resuspended in 300 µL of 50 mM ammonium bicarbonate (ABC) buffer. Proteolytic digestion was performed by adding 1 µg of Trypsin/Lys-C mix (Promega Corporation, MA, USA) per sample and digestion was carried out overnight at 37 °C under gentle agitation. Next, the digestion was quenched by acidification with 45 µL of 5% trifluoroacetic acid, and peptide samples were transferred to EvoTips (Evosep) as a purification and concentration step. Finally, the purified peptide eluates were dried using a SpeedVac concentrator and stored at -80 °C until LC-MS/MS analysis.

Prior to LC-MS/MS analysis, samples were resuspended in 30 µL of 0.1% formic acid in water. Peptide separation and analysis were performed using a timsTOF Pro QTOF mass spectrometer (Bruker, Billerica, MA, USA) coupled to a nanoElute UHPLC system (Bruker). Chromatographic separation was carried out on a C18 PepSep analytical column (150 mm × 75 µm, 1.9 µm particle size, 120 Å pore size; Bruker Daltonics, Bremen, Germany). Peptides were eluted using a 30-minute linear gradient from 2% to 35% solvent B (0.1% formic acid in acetonitrile), followed by a 3-minute increase to 95% B, and a 7-minute wash phase at 95% B. The flow rate was maintained at 250 nL/min, and the column temperature was set to 40 °C. Data acquisition was conducted in diaPASEF mode, following the method described by Arenas-De Larriva et al. (2022).

Raw diaPASEF files were processed with the software DIA-NN v2.0 (Demichev et al. 2020). Protein identification was obtained by searching against the Mus musculus SwissProt-reviewed FASTA database (17,226 canonical proteins, 13 September 2023) with default parameters except for several optimized settings: prediction of peptide properties using deep learning (MS/MS spectra, RTs, IMs); allowance of up to two missed cleavages; fixed modification of carbamidomethylation on cysteine (C); variable modifications including methionine oxidation [Ox(M)] and N-terminal acetylation [Ac(N-term)]; enabling of N-terminal methionine excision; analysis at the peptidoform level and inclusion of protein names from FASTA; a precursor charge range of 2–5; precursor false discovery rate (FDR) set at 1%; MS1 and general mass accuracies set at 15 ppm; ultra-precise quantification mode (Quant UMS, high accuracy); cross-validated neural networks (NNs); RT-dependent profiling, smart profiling, and optimal results settings activated; and match-between-runs enabled. The resulting proteinGroup.txt file was loaded onto Perseus v 1.6.15 (Tyanova et al. 2016) for further data processing and statistical analysis. First, a missing value filter was applied, removing all protein groups with more than 30% missing values (NA), corresponding to a 70% valid value threshold. Second, data were log2 transformed and the remaining missing values were imputed to preserve data structure and enable downstream comparative analysis.

Functional analysis of the proteins identified only in the IP samples was performed using String (www.string-db.org). The functional graph was obtained with Iulius AI (Julius AI | Your AI Data Analyst).

Transcriptomic microarray

AlphaTC1.9 cells were transfected as described above, and the isolated RNA (1 µg) was subjected to a cDNA microarray analysis on the ClariomTM S Array (Thermo Fisher Scientific). Data were acquired on the GeneChipTM 3000 instrument (Affymetrix, Santa Clara, California, USA) and high-throughput automated processing was performed using the GeneTitan™ Microarray System (Thermofisher). To evaluate differential gene expression, raw data were normalized and analyzed at the gene level using the RMA algorithm included in the Transcriptome Analysis Console (TAC). Microarray analyses were performed on three biologically independent RNA replicates per experimental group. Microarray raw data were pre-processed using the Robust Multi-array Average (RMA) algorithm to normalise the data, correct for background noise and summarise across arrays using transcript clusters containing safely annotated genes (Carvalho and Irizarry 2010). Differential gene expression analysis was conducted by means of empirical Bayes moderated t-statistics. Genes with an FDR-adjusted p-value < 0.05 and a log2(Fold Change) > |1| were considered differentially expressed (Ritchie et al. 2015). Functional enrichment analysis was performed on the identified gene sets to explore biological pathways and gene ontology (GO) terms enriched among the DE genes (Bioconductor). Statistical significance was assessed by means of Fisher test with modifications (Alexa et al. 2006).

Cell Immunofluorescense for confocal and STORM imaging

AlphaTC1.9 cells were seeded at a density of 3,000 cells per well in cell chambers (Ibidi, Germany) and were fixed at 50% confluence.

Cells were incubated for 1 h at RT with blocking buffer (5% normal goat serum (NGS), 0.1% Triton X-100, 0.01% unconjugated affinity-purified F(ab) fragment anti-mouse IgG) in PBS. Following blocking, cells were incubated with primary antibody for 1 h at RT; anti-IDE (1:50, #AB9210; Millipore), anti-acetylated tubulin

(1:750, #T6793; Sigma-Aldrich), anti-Golga2 (1:100, #HPA021799; Atlas Antibodies), anti-GM130 (1:100, #610823; Becton Dickinson). Samples were washed three times with PBS and subsequently incubated with secondary antibodies CF583 (1:100, #20792–50 µl (Biozol) and CF505 (1:100, #20877–50 µl (Biozol)) for 1 h at RT in the dark. Cells were washed five times with PBS and incubated with 4% PFA for 10 min at RT in the dark. If images were acquired using the confocal microscope, a Hoechst staining step was performed (omitted for STORM imaging).

Immunofluorescence of pancreatic sections

Pancreatic sections (4 µm thick) from A-IDE-KO and A-IDE-WT mice were immersed twice in tissue clearing agent for 10 min each, and subsequently rehydrated in ethanol. Antigen retrieval was performed using pH 6 citrate buffer, in a pressure cooker for 20 min.

Subsequently slides were incubated with Fab blocking solution (PBS, 5% goat serum, 1% Fab mouse blocking reagent) for 1 h at RT. Next, slides were washed in PBS-T (PBS 0.01% Tween-20). Primary antibodies were incubated for 1 h at room temperature: Insulin (1:10, #IS00230-2, Agilent Technologies), Glucagon (1:1,000, #ab92517, Abcam) and Acetylated tubulin (1:1,200, #T6793; Sigma-Aldrich). After primary antibody incubation, slides were washed in PBS-T. Secondary antibody staining was performed using Alexa Fluor-conjugated secondary antibodies for 30 min at RT in the dark: AF488 (1:1,000, #A1107, Life Technologies), AF647 (1:1,000, #A21242; Life Technologies), AF555 (1:1,000, #A21430; Life Technologies). Slides were washed afterwards. Nuclei were counterstained with Hoechst.

Stochastic optical reconstruction microscopy (STORM)

To visualize cilia with a resolution of 20–30 nm, we used STORM microscopy. Once the samples were immunostained, BCubed imaging buffer (ONI, Oxford, UK) was applied to the sample. Single molecule data acquisition (SMLM) was conducted on the Nanoimager S running NimOS V.1.19.4 (ONI, Oxford, UK). The images were acquired using a 100 × 1.4 NA objective lens (Olympus, Japan) and a sCMOS camera (Hamamatsu Orca Flash 4.0 V3). Each acquisition was conducted with the exposure time set at 30ms, with the temperature control enabled and set at 32 °C. The 561 nm laser was used to image the CF583 dye, while the 466 bn laser was used to image the CF505 dye. A total of 30,000 image frames were captured (10000 per laser), using a high-sensitivity sCMOS camera. The microscope was equipped with a 100x oil immersion objective (Olympus UPLXAPO100) with a numerical aperture of 1,4 and working distance of 0,13 mm. For image reconstruction, the NimOS processing software (ONI, Oxford, UK) was used. Drift correction, localization filtering and some data analyses were performed in the data analysis platform from the microscope manufacturer (CODI, ONI, Oxford, UK). Drift was corrected over all frames and included all localizations with photon count < 30,000, SD of the point-spread function between 75 nm and 200 nm, estimated localization precision (SD) <15 nm. Localizations were excluded where the same emission event lasted more than 15 frames.

Confocal microscopy

ONI Nanoimager was also employed for confocal microscopy. The acquired confocal images were processed separately from the STORM data. Cilia length were quantified using the free ImageJ software (NIH, USA). For colocalization analysis, the Jacob plugin was used, and the Pearson correlation coefficient was applied.

Statistical analysis

Statistical analysis of data was performed using Prism v.6.0 (GraphPad Software). Distributions were checked with the Kolmogorov-Smirnov test. Data are presented as means ± SEM. Comparisons between two groups were done using the unpaired Students' t-test. Comparisons between more than two groups were first assessed using a two-way ANOVA, and then Bonferroni post-hoc test. Differences were considered significant at $p < 0.05$.

Results

A proteomics study involving IDE Immunoprecipitation revealed implications in cytoskeleton and cellular projection

Three independent immunoprecipitation (IP) samples (using an anti-IDE antibody in pancreatic alpha-cell extracts) and their respective controls were analyzed using LC-MS/MS. 683 proteins were detected in the three IP samples analyzed, but not in the controls. Only those proteins identified by two or more peptides were considered, resulting in a final number of 513 proteins. Among these, we found the IDE protein, which confirmed the quality of the IP assay. The full list of proteins identified in the immunoprecipitation assay can be found in Supp. Table 1.

A functional analysis was carried out with String-DB online platform, in order to identify potential interactor partners of IDE (Supp. Tables 2 and 3). A selection of the most representative functions identified for the IDE-interacting proteins have been represented in Fig. 1A. Among them, there were many proteins related with the cytoskeleton, cellular organization and projection, as well as proteins related to mitochondrial function or glucose and lipid metabolism. Finally, IDE itself was also associated with spliceosomes, RNA splicing, oxidative stress and Alzheimer disease. The functional network including

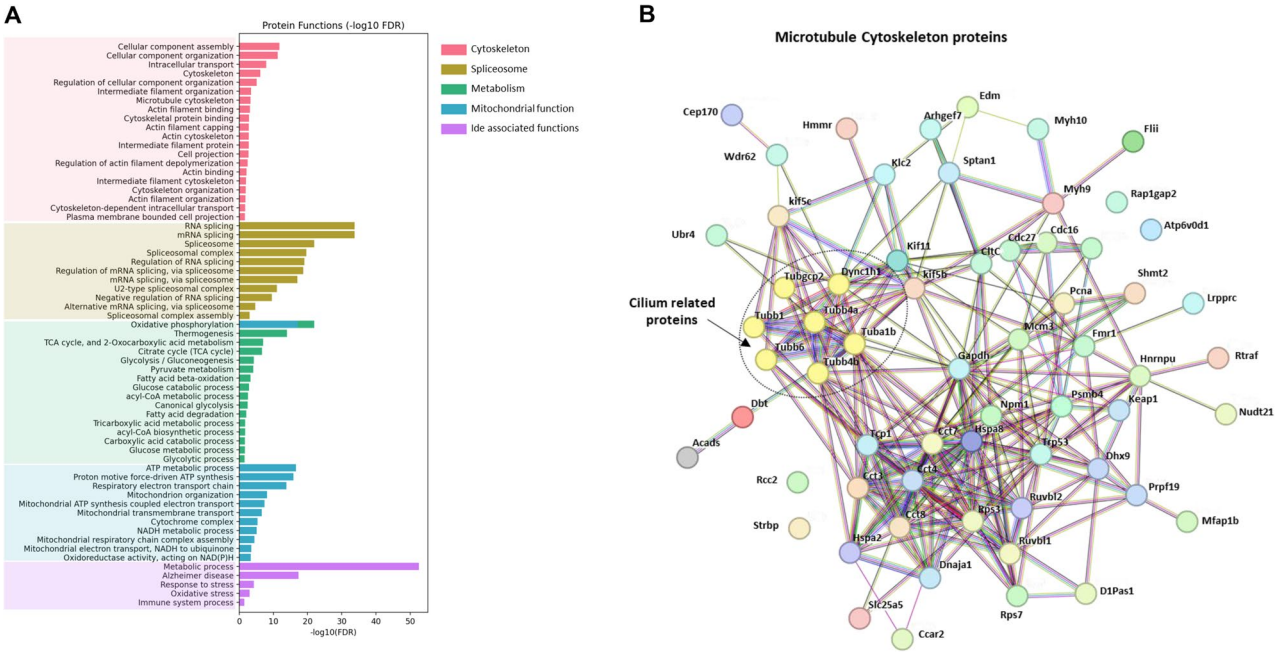

Fig. 1 Proteomics of IDE immunoprecipitation. **A** IDE- interacting proteins identified by LC-MS/MS were associated to several biological functions. The most representative are shown, included into 5 main groups: cytoskeleton, splicesome, metabolism, mitochondrial function and known IDE-associated functions. **B** Proteins related to microtubule tubulin cytoskeleton, including some cilium related proteins were represented as a network, provided by String online platform

proteins associated with the microtubule cytoskeleton and primary cilium (Tubb1, Tuba1b, Tubb6, Tubb4a, Tubb4b, Dynchn1…) is shown in Fig. 1B. These data supported the notion that the tubulin cytoskeleton and the primary cilia are relevant to the function of IDE in pancreatic alpha-cells.

We chose to study one of the cytoskeletal proteins obtained in the proteomics, Dync1h1 (cytoplasmic dynein 1 heavy chain 1). It was select because *Dync1h1* heterozygous mice show decreased levels of glucagon in plasma along with a metabolic phenotype (Eschbach et al. 2013). Thus, we generated a knock-down model using *Dync1h1* (Dync) siRNA with 90% decrease in protein expression, interestingly Dync-KD cells didn´t show effects on glucagon secretion, pointing to a dispensable role of this protein in alpha-cell function (Supplementary Fig. 2).

Then, instead of focusing on specific proteins, we decided to explore one of the biological functions revealed by the proteomic study: microtubule cytoskeleton and the primary cilium. To do so, we used an IDE knock-down model, as explained next.

The loss of IDE expression in alpha-cells leads to impaired ciliogenesis

We first generated the alpha-cell IDE-KD model using siRNA to silence *Ide* expression. IDE was knocked-down ~25% as detected by protein levels and ~75% as detected by mRNA levels (Fig. 2A-C) leading to a ~30% decrease in cilia number and length when compared to control (siRNA-scramble) (Fig. 2D-F). Altogether these results support the idea that IDE has a direct relationship with the primary cilium.

IDE-KD cells and controls were used to perform a transcriptomic array. This revealed that genes involved in ciliogenesis and other related membrane components exhibited differential expression when IDE was diminished (Supplementary Fig. 3). This finding is in line with our previous observations in Figs. 1 and 2.

To investigate whether IDE is part of the primary cilium structure, we performed immunostaining on alphaTC1.9 cells using antibodies for acetylated tubulin and IDE. Representative images from confocal microscopy (Fig. 2G) and STORM (Fig. 2H) demonstrate that IDE is not localized within the primary cilium.

A loss of IDE expression in alpha-cells leads to dysregulated glucagon secretion and the loss of insulin-inhibitory signals

Glucagon secretion by IDE-KD cells was impaired under low glucose conditions (Fig. 3A). Furthermore, insulin treatment did not inhibit glucagon secretion any further in IDE-KD cells (Fig. 3B). These results are consistent with the decreased protein levels of the insulin receptor (IR) observed in the IDE-KD cells compared to the control cells (Fig. 3C-D), which is not due to transcriptional regulation as shown by RT-PCR results (Fig. 3E). Finally, we stimulated IDE-KD and control cells with 100nM insulin to induce downstream signaling. We

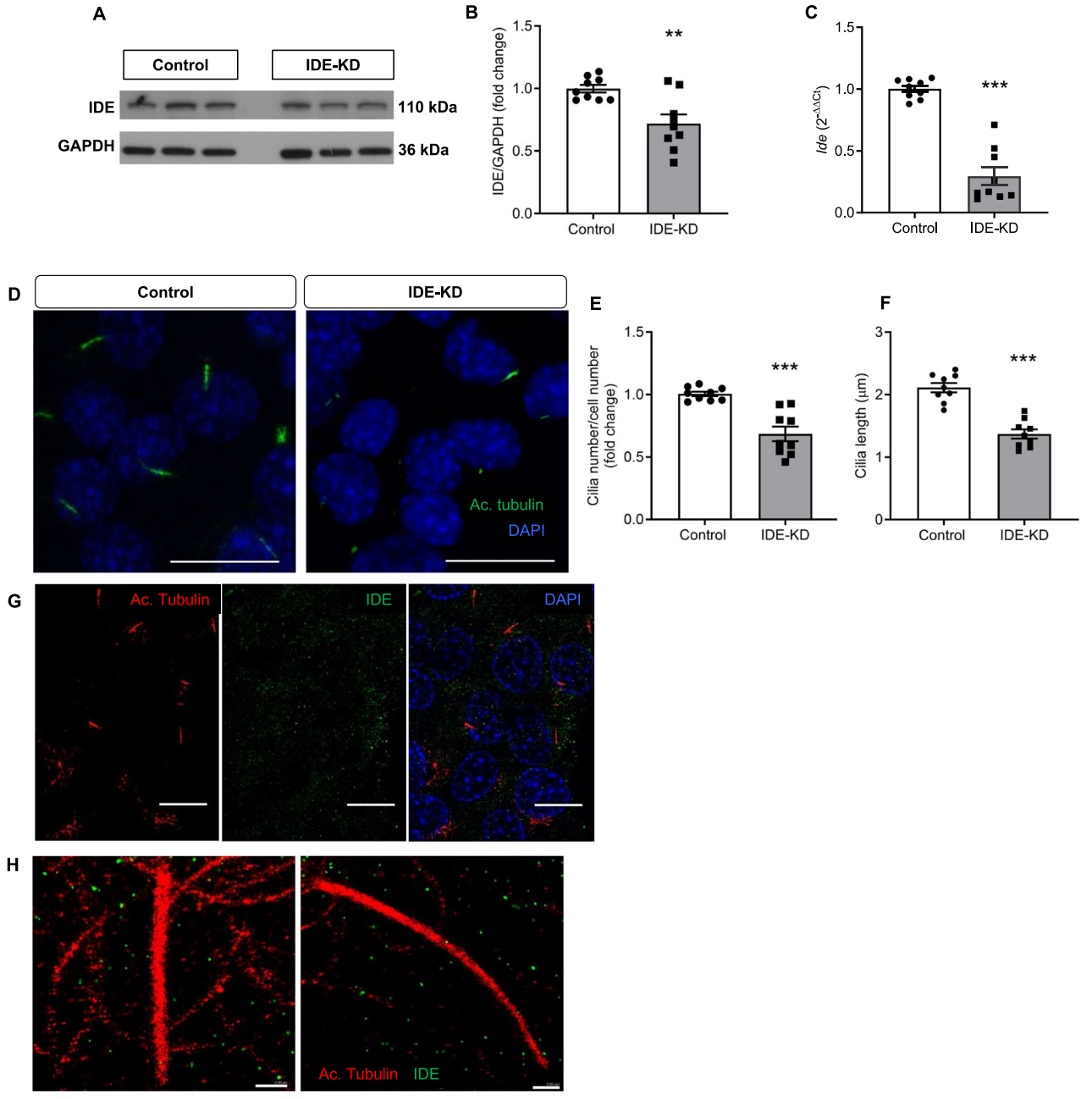

Fig. 2 Impaired ciliogenesis in IDE-knock-down alphaTC1.9 cells. **A** Representative western-blot analysis of IDE after 48 h of siRNA-IDE (IDE-KD) and siRNA-scramble (control) transfection. **B** Quantification of IDE/GAPDH in IDE-KD and control cells, $N=9$. **C** Quantification of Ide gene expression by RT-PCR, $N=9$. **D** Representative immunostaining of acetylated tubulin staining in IDE-KD and control cells. **E** Quantification of cilia number and, **F** cilia size, $N=9$. **G** Representative confocal microscopy images showing IDE and acetylated tubulin (primary cilia) and DAPI (nucleus). Graph bar= 10 µm. **H** Representative STORM images showing further details of colocalization observations. Graph bar = 0.5 µm. $^{**}p<0.01$, $^{***}p<0.001$. Data are represented as mean ± SEM

then detected pIR and plotted a time response curve of pIR/GAPDH. We found that pIR decreased ($p=0.07$) in IDE-KD cells (Fig. 3F-H). We did not perform a pIR/IR ratio analysis in this study because IR levels were modified from baseline (time 0) due to IDE loss, as previously demonstrated (Fig. 3C-D). These results indicate the existence of insulin resistance in IDE-KD alpha-cells.

A second model of IDE knock-down (shIDE) in alpha-TC1.9 cells was generated using lentivirus containing shRNA-IDE and empty lentivirus as control (shControl), 50% diminished expression was obtained as measured by protein levels and RT-qPCR. Glucagon secretion in this model was similar to the siRNA-IDE (Supplementary Fig. 4). Unexpectedly, we observed a discrepancy in glucagon secretion responses between

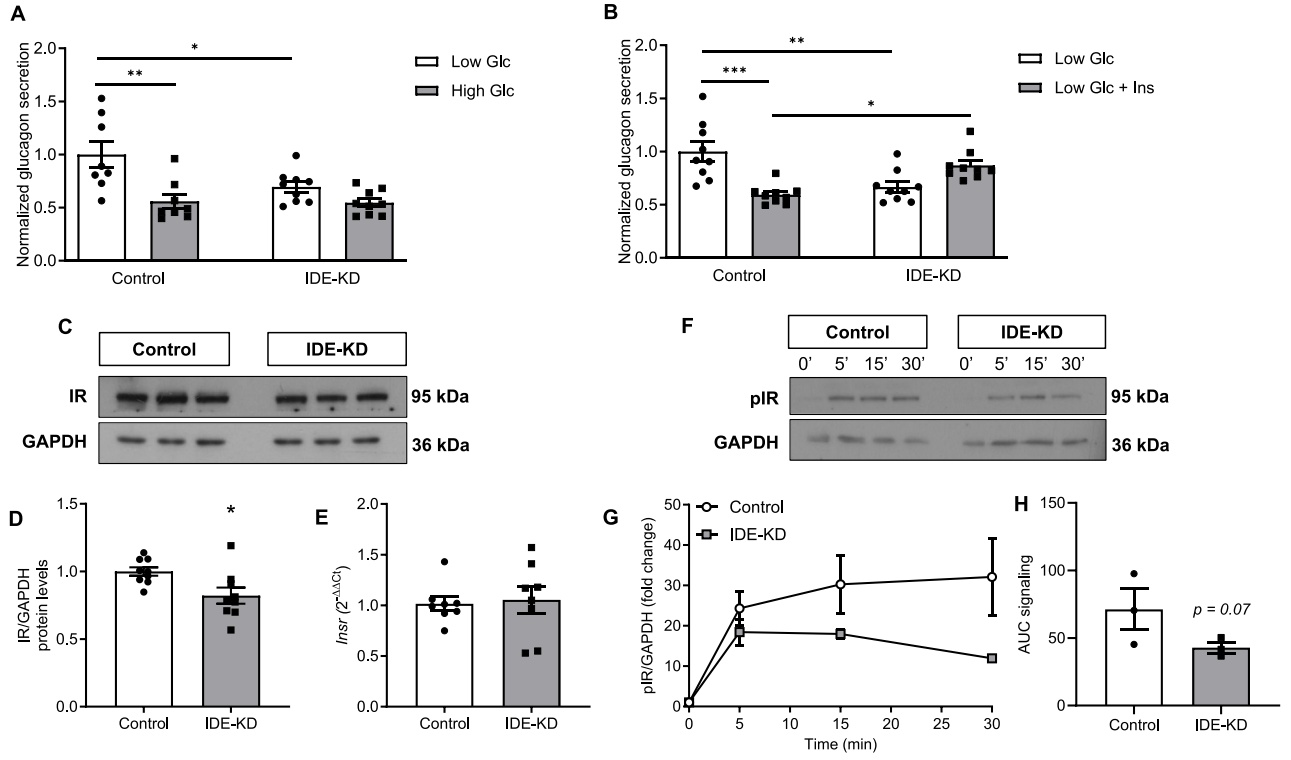

Fig. 3 Impaired glucagon secretion and insulin receptor levels in IDE-KD cells. **A** Low glucose (1 mM) stimulates glucagon secretion in alphaTC1.9 cells meanwhile high glucose (16 mM) inhibits it in control cells, meanwhile, IDE-KD cells have lost glucagon secretion capacity at low glucose, $N=9$. **B** Low glucose stimulated glucagon secretion is inhibited by 100nM insulin in control cells, this inhibition is lost in IDE-KD cells, $N=9$. **C** Representative IR western-blot of control and IDE-KD protein extracts. **D** Quantification of IR protein levels in IDE-KD compared to control cells, $N=9$. **E** Quantification of Insr gene expression by RT-PCR, $N=9$. **F** Representative pIR western-blot after insulin stimulation for 5, 15 and 30 min. **G** Quantification of pIR dynamic between 0- and 30-minutes post-insulin stimulus, $N=3$. **H** Area under the curve (AUC) quantification to measure differences in insulin signalling between WT and IDE-KD cells. *$p<0.05$ **$p<0.01$, ***$p<0.001$. Data are represented as mean ± SEM

the A-IDE-KO (Merino et al. 2022) and IDE-KD alpha-cell models (Fig. 3 and Supplementary Fig. 4), despite both models exhibiting impaired glucose sensing in alpha-cells. To study the cause of this difference, we performed glucagon secretion tests on islets isolated from heterozygous alpha-cell-specific IDE mice (A-IDE-HT), with partial loss of IDE expression (as IDE-KD cells) but with intact paracrine signals surrounding alpha-cells. A-IDE-HT islets, which had experienced a partial loss of IDE expression, exhibited a secretory profile similar to that of A-IDE-KO islets (Supplementary Fig. 5A), suggesting that the cause of the differential glucagon secretion pattern in the cell line versus the pancreatic islets is not the ´partial´ *versus* ´total´ loss of IDE, but rather the paracrine regulation by non-alpha cells. In fact, alpha-cells of A-IDE-HT islets miss insulin inhibitory control (Supplementary Fig. 5B) and insulin secretion is constitutive in the A-IDE-HT islets (Supplementary Fig. 5C).

Two models of impaired ciliogenesis in alpha-cells show dysregulated glucagon secretion and impaired insulin regulation

In light of our previous findings, we hypothesize that the primary cilium plays a pivotal role in alpha-cell function. To confirm this, we have developed two models of impaired ciliogenesis: ARL13B (ARL13B-KD) and IFT88 knock-down (IFT88-KD), two proteins that are required for normal ciliogenesis.

To generate the ARL13B-KD model, we performed transfections using siRNA. ARL13B was knocked-down by ~70%, as determined by protein levels (Fig. 4A–B), and ~45% as detected by mRNA levels (Fig. 4C) resulting in a ~30% reduction in cilia number and a ~10% decrease in cilia length (Fig. 4D-F) in alpha-cells. A second model of impaired ciliogenesis was generated using IFT88 siRNA, which decreased IFT88 protein levels by ~60% (Fig. 4G-H) and ~45% as detected by mRNA levels (Fig. 4I) and primary cilium number by 60% (Fig. 4J-K), with no change in cilia length (Fig. 4L). Loss of ARL13B expression resulted in impaired glucagon secretion when alpha-cells were treated with a low-glucose medium

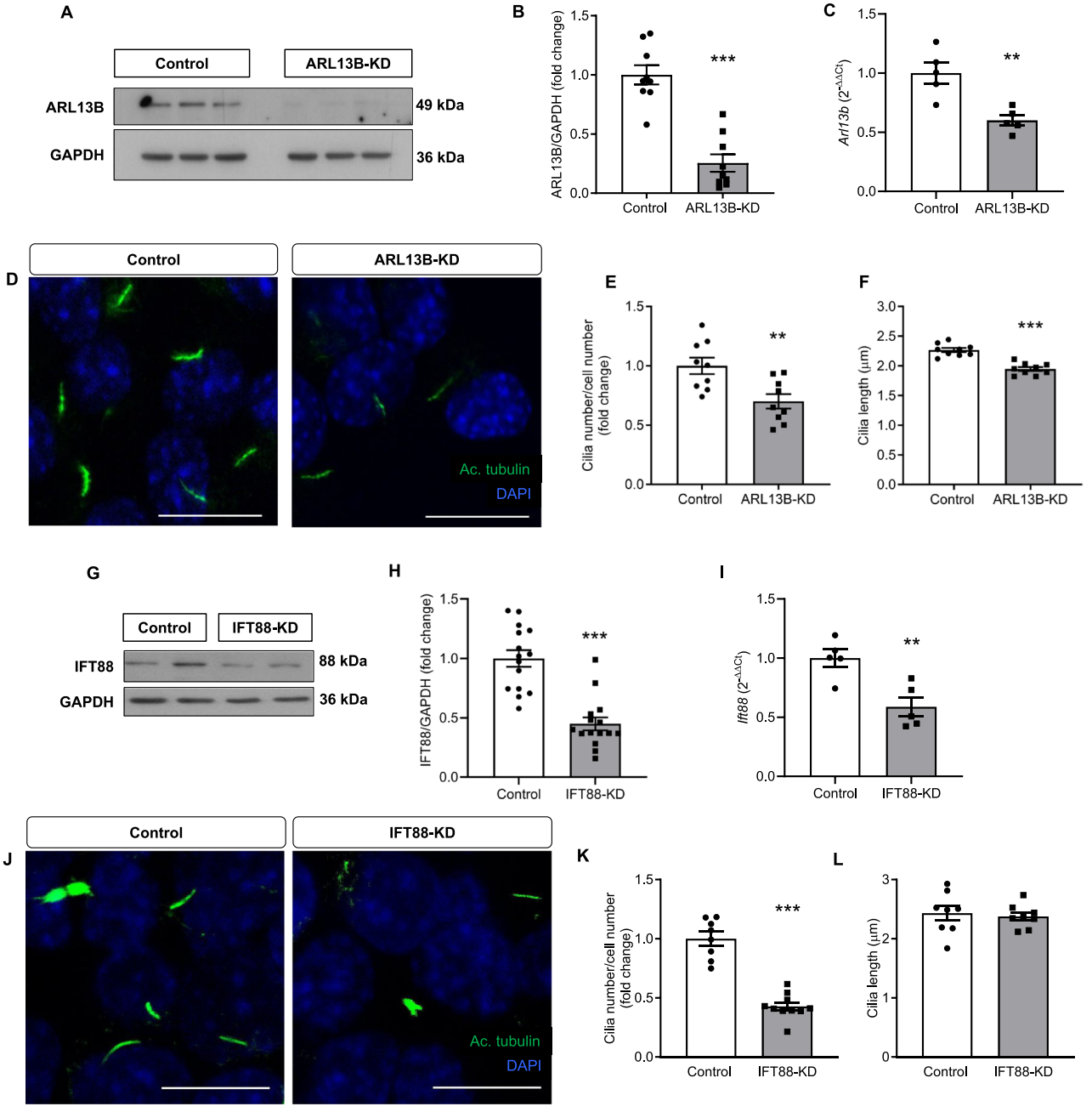

Fig. 4 Impaired ciliogenesis in ARL13B-knock-down and IFT88-knock-down alphaTC1.9 cells. **A** Representative western-blot analysis of ARL13B after 48 h of siRNA-ARL13B (ARL13B-KD) and siRNA-scramble (control) transfection. **B** Quantification of ARL13B/GAPDH in ARL13B-KD and control cells, $N=9$. **C** Quantification of Arl13b gene expression by RT-PCR, $N=6$. **D** Representative immunostaining of acetylated tubulin staining in ARL13B-KD and control cells. **E** Quantification of cilia number and, **F** cilia size, $N=9$. **G** Representative western-blot analysis of IFT88 after 48 h of siRNA-IFT88 (IFT88-KD) and siRNA-scramble (control) transfection. **H** Quantification of IFT88/GAPDH in IFT88-KD and control cells, $N=15$. **I** Quantification of Ift88 gene expression by RT-PCR, $N=6$. **J** Representative immunostaining of acetylated tubulin staining in IFT88-KD and control cells. **K** Quantification of cilia number and, **L** cilia size, $N=8$–10. $^{**}p<0.01$, $^{***}p<0.001$. Data are represented as mean ± SEM. Graph bar= 10 µm

(Fig. 5A). This is consistent with what happens in the IFT88-KD model (Fig. 5B).

Interestingly, both models of impaired ciliogenesis exhibited impaired insulin action (Fig. 6A-B) and decreased IR protein levels by ~30–40% (Fig. 6C-D and F-G) which is not due to transcription regulation (Fig. 6E, H). These results support the idea that loss of paracrine insulin signaling occurs when the primary cilium is impaired. They also suggest the possibility of insulin resistance in the absence of primary cilium of alpha-cells.

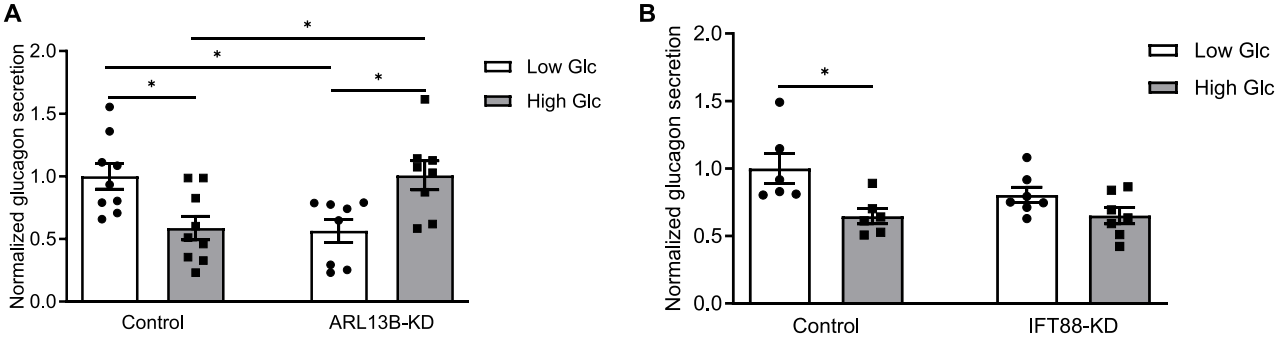

Fig. 5 Impaired glucagon secretion in ARL13B-KD and IFT88-KD cells. **A** Low glucose (1mM) stimulates glucagon secretion in alphaTC1.9 cells meanwhile high glucose (16mM) inhibits it in control cells, meanwhile, ARL13B-KD cells have lost glucagon secretion capacity at low glucose, $N=9$. **B** IFT88-KD cells have lost glucagon secretion capacity at low glucose, $N=6$. *$p<0.05$. Data are represented as mean ± SEM

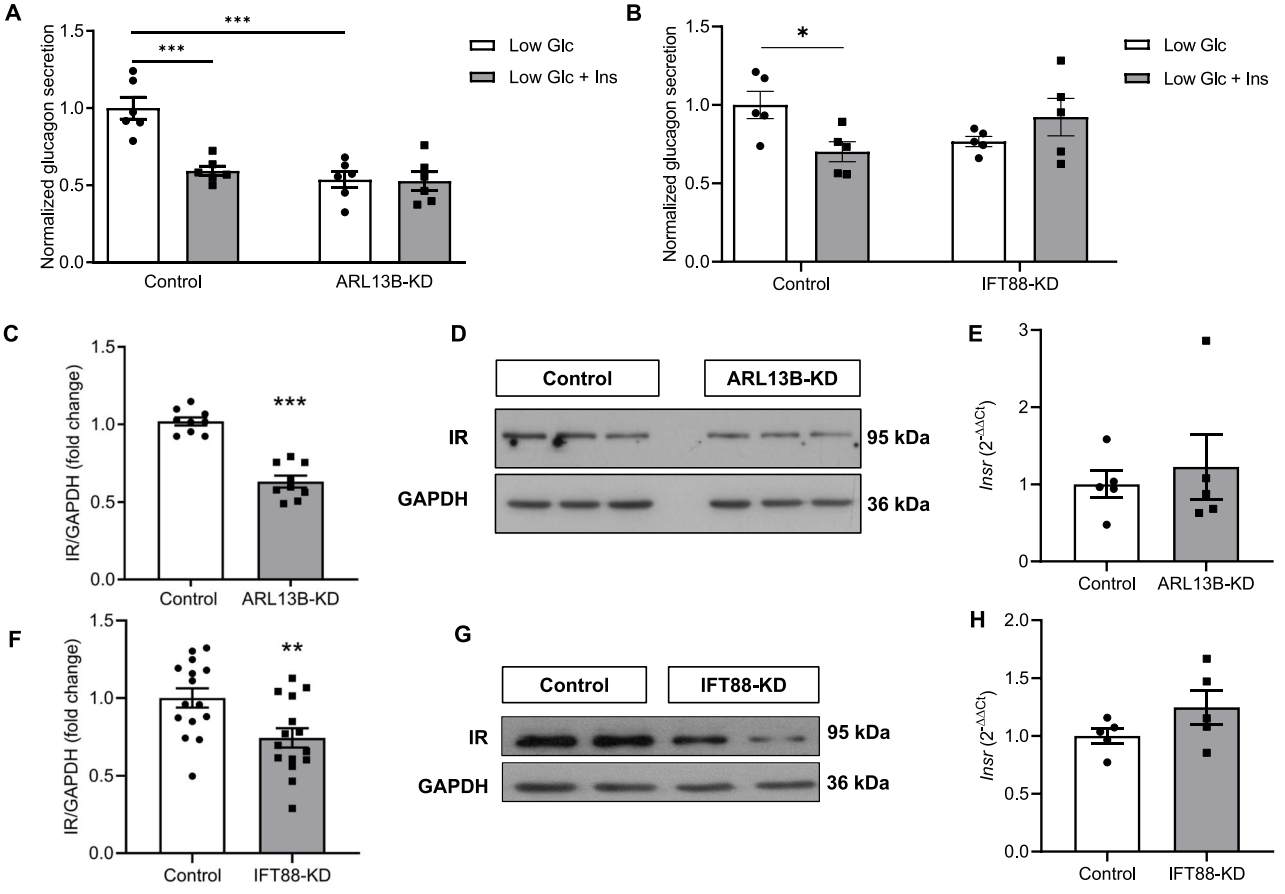

Fig. 6 Impaired insulin action and insulin receptor levels in ARL13B-KD and IFT88-KD cells. **A** Insulin inhibits glucagon secretion at 1mM glucose in alphaTC1.9 cells, meanwhile insulin inhibition is lost in ARL13B-KD cells, $N=9$. **B** Insulin inhibits glucagon secretion at 1mM glucose in alphaTC1.9 cells, meanwhile insulin inhibition is lost in IFT88-KD cells, $N=5$. **C** Insulin receptor levels are decreased in ARL13B -KD cells in respect to control. **D** Representative western-blot of IR in ARL13B -KD and control cells. **E** Quantification of *Insr* gene expression by RT-PCR, $N=6$. **F** Insulin receptor levels are decreased in IFT88-KD cells in respect to control, $N=15$. **G** Representative western-blot of IR in IFT88-KD and control cells. **H** Quantification of *Insr* gene expression by RT-PCR, $N=6$. **$p<0.01$, ***$p<0.001$. Data are represented as mean ± SEM

The inhibitory phase of glucagon secretion is similar to the inhibition of IDE expression and the regulation of primary cilium

To investigate the relationship between physiological glucagon secretion and IDE levels, as well as downstream events related to tubulin and primary cilium dynamics, we assessed glucagon secretion in alphaTC1.9 cells. The cells were incubated with low (1 mM) and high (16 mM) glucose levels for 30 min, stimulatory and repressive glucagon secretion conditions respectively. Afterwards,

media were collected and glucagon secretion/ inhibition assessed (Fig. 7A). In addition, cells were lysed and by Western blotting we detected, IDE, two primary cilium markers (ARL13B and acetylated tubulin), alpha-tubulin, and IR levels. Interestingly, under conditions of high glucose, IDE, both cilia markers, alpha-tubulin and IR levels were decreased by ~25%, ~60%, ~25% and ~25%, respectively (Fig. 7B-C).

These results suggest that downregulation of IDE is a prerequisite for inhibiting glucagon secretion, which is consistent with the results of IDE-KD. Similarly, decreased levels of tubulin acetylation and ARL13B suggest diminished ciliogenesis. Interestingly, insulin receptor protein levels were also decreased. Taken together, these results can be indicating a series of dynamic events in which IDE acts as a glucose sensor controlling tubulin and primary cilium dynamics in order to regulate glucagon secretion.

A-IDE-KO hyperglucagonemic mice show impaired alpha-cell ciliogenesis and decreased tubulin levels in pancreatic islet cells

A-IDE-KO mice displayed hyperglucagonemia, while ex vivo, dysregulated glucagon secretion was shown by A-IDE-KO isolated islets (Merino et al. 2022). Based on the previous results of the present manuscript, we aimed to investigate the primary cilium of A-IDE-KO mice in vivo, and the tubulin cytoskeleton using A-IDE-KO isolated islets.

Herein, we have stained pancreata from A-IDE-KO mice and controls (A-IDE-WT) with acetylated tubulin, glucagon and insulin in order to detect and quantify primary cilium of alpha- and beta-cells respectively (Fig. 8A). Interestingly, we found a ~20% decrease in alpha-cells primary cilia number in the A-IDE-KO pancreata when compared to A-IDE-WT (Fig. 8B) and no changes in beta-cell cilia number. Isolated islets from these mice were used for protein extraction and Western blotting to detect the expression of two ciliary markers (ARL13B and acetylated tubulin) and alpha-tubulin (Fig. 8C). Quantification of those western-blots showed ~40% decrease on the expression of ciliary markers (Fig. 8D-E) and ~50% decrease in alpha-tubulin (Fig. 8F) in A-IDE-KO islets versus controls. These in vivo data supported the relevance of tubulin cytoskeleton and primary cilium in alpha-cell function, and it reinforced the notion that IDE plays a role in the regulation of alpha-cell ciliogenesis.

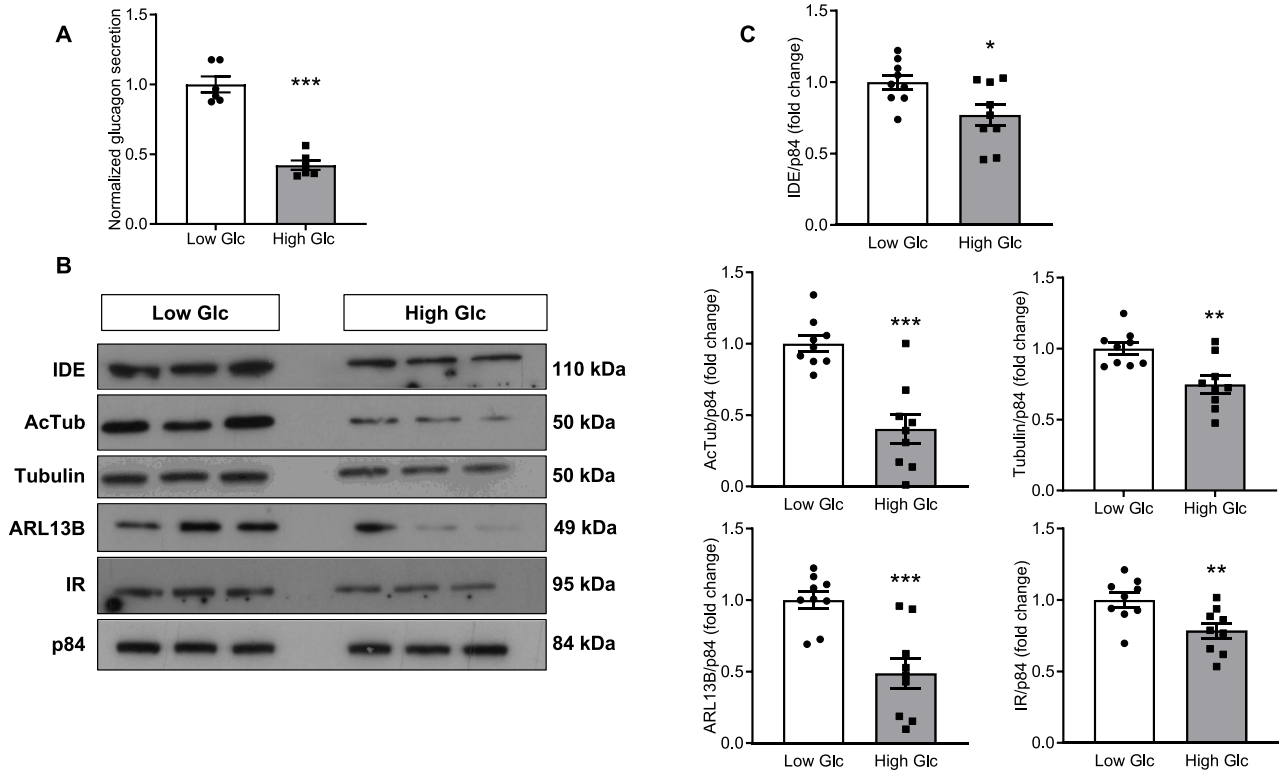

Fig. 7 IDE and primary cilium dynamics under glucose-regulated glucagon secretion and inhibition. **A** Glucagon secretion in wild type cells (alphaTC1.9) under conditions of low (1mM) and high (16mM) glucose. **B** Representative western-blots for IDE, acetylated tubulin (AcTub), tubulin, ARL13B, insulin receptor (IR) and the nuclear protein p84. **C** Quantification of IDE protein levels, tubulin acetylation, alpha-tubulin, ARL13B, IR and p84 (housekeeping), $N=9$. *$p<0.05$ **$p<0.01$, ***$p<0.001$. Data are represented as mean ± SEM

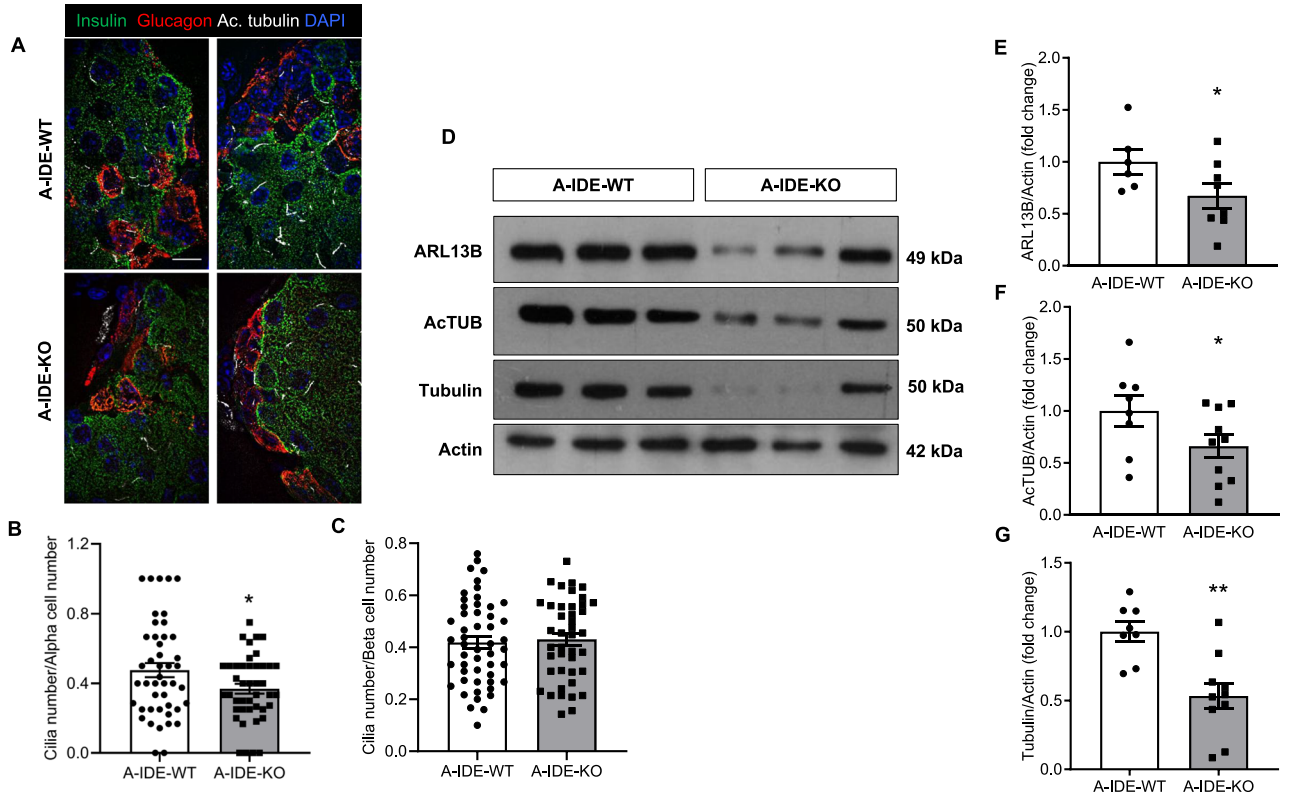

Fig. 8 Impaired ciliogenesis in pancreatic alpha-cells of A-IDE-KO mice. **A** Representative pictures of insulin (green), glucagon (red), acetylated tubulin (white) and DAPI (blue) in A-IDE-WT ($N=4$) and A-IDE-KO ($N=4$) mouse pancreata. **B** Quantification of cilia number per alpha-cell number. **C** Quantification of cilia number per beta-cell number. **D** Representative western-blot analysis of ARL13B, acetylated tubulin (AcTUB), alpha-tubulin and actin in A-IDE-KO isolated islets and controls. **E** Quantification of ARL13B, **F** AcTUB, and, **G** alpha-tubulin western-blots (normalized to actin), A-IDE-WT ($N=6$) and A-IDE-KO ($N=8$). *$p<0.05$. Data are represented as mean ± SEM. Graph bar= 10 µm

Discussion

In diabetes mellitus, glucagon secretion is inappropriately high for several reasons, including dysregulation of alpha-cell function and impaired paracrine insulin suppression. Hyperglucagonemia further promotes hyperglycemia by activating glycogenolysis and gluconeogenesis in the liver. The mechanisms underlying hyperglucagonemia in diabetes are poorly understood. In this regard, we have reported that IDE is important in the physiological regulation of glucagon secretion, and its loss of expression in vivo leads to hyperglucagonemia and constitutive glucagon secretion (Merino et al. 2022).

Conversely, the counter-regulatory mechanisms of hypoglycemia progressively decline in type 1 diabetes, resulting in the failure to activate glucagon secretion and maintain euglycemia. Therefore, dysregulation of glucagon secretion is an important feature of hyperglycemia and hypoglycemia.

Although several authors have described the molecular mechanisms that regulate glucagon secretion by pancreatic alpha-cells, no consensus has yet been reached on this issue (Gilon 2020; Wendt and Eliasson 2020). Briefly, during hypoglycemia, the rate of glucose uptake via the high-affinity glucose transporter GLUT1 is low. Glucose is then metabolized to increase the ATP/ADP ratio modestly, leading to the partial closure of ATP-sensitive potassium (KATP) channels. This maintains the membrane potential of the alpha-cell sufficiently depolarized to allow action potential (AP) firing, thereby preventing voltage-dependent inactivation of voltage-gated Na^+ channels. The resulting high-amplitude AP activates P/Q-type calcium channels triggering exocytosis of glucagon-containing secretory granules (Gao et al. 2023). However, there is still a knowledge gap regarding the regulation of glucagon secretion, and IDE appears to be involved in some of these unexplored mechanisms, as was previously demonstrated by our research group (Merino et al. 2022).

Primary cilia in pancreatic beta-cells are essential organelles for insulin secretion, islet communication and glucose homeostasis (Muller et al. 2024; Volta et al. 2019; Cho et al. 2022). However, its role on glucagon secretion in alpha-cells is completely unknown. In this study, we used immunoprecipitation proteomics, a biochemical technique that can be used for studying the interactions between proteins and their binding partners, including cytoskeletal proteins, and those involved in

cilia formation and function. Immunoprecipitation proteomics using an anti-IDE antibody revealed interesting and unexpected results. We have focused on the tubulin cytoskeleton and the primary cilium due to the importance of microtubules in the structure of the axoneme, which is necessary for the formation of the primary cilium. Thus, IDE interacts with Dync1h1 a cytoplasmic dynein indispensable for the assembly, maintenance, and function of the primary cilium, mainly through its role in retrograde intraflagellar transport and cytoskeletal organization (Sakamoto et al. 2024; Edwards 1990; Zhou et al. 2025). Additionally, we found several β-tubulins (TUBB1, TUBB4B, TUBA1B) and γ-tubulin (TUBGCP2) which are fundamental for the assembly, stability and function of the primary cilium (Khan et al. 2022; Sewell et al. 2024; Hao et al. 2021; Shankar et al. 2022). Exploration of the function of Dync1h1 in alpha-cells did not reveal a significant role for this protein in glucagon secretion. This suggests that the biological functions identified, through proteomics of IDE interactome, give more information on IDE molecular mechanisms than the specific and single proteins.

In the last decade, intra-islet paracrine signals have emerged as a key factor in regulating the function of islet cells (Hartig and Cox 2020). In this context, insulin signalling plays a pivotal role in regulating alpha-cell function in vivo, by inhibiting glucagon secretion through the activation of the classical IR/PI3K/AKT pathway (Kawamori et al. 2009). This is a signal for recruitment of the $GABA_A$ receptor to the membrane and induction of Cl^- influx, which leads to hyperpolarization and inhibition of glucagon exocytosis (Xu et al. 2006). Our previous results (Merino et al. 2022) using isolated islets of A-IDE-KO mice, and the results in Supplementary Fig. 5B using isolated islets of A-IDE-HT show impaired inhibition of insulin on glucagon secretion when IDE expression is diminished (independently of total or partial loss). In the current manuscript, we demonstrate that loss of insulin regulation is due to insulin resistance caused by reduced IR levels and impaired insulin signaling. Interestingly, loss of IR was recapitulated in both models of cilium impairment, suggesting the presence of IRs in the primary cilium. This hypothesis is intriguing and supported by few articles reporting tyrosine kinase receptors in the primary cilium (Yeh et al. 2013; Gerdes et al. 2014; Christensen et al. 2017), which maybe using non-canonical pathways regarding to the IGF1R (Yeh et al. 2013). These authors described important functions for ciliary IGF1 signaling, related to primary cilium disassembly in order to enter the cell cycle. This provocative study led us to consider the potential localization of a subpopulation of IR in the primary cilium of alpha-cells. This possibility was confirmed by Gerdes et al. who demonstrated the presence of insulin receptors in the primary cilium of pancreatic beta-cells, after insulin stimulation. They postulated that ciliary function is implicated in insulin secretion and insulin signaling in the beta-cell, and that ciliary dysfunction could contribute to type 2 diabetes susceptibility (Gerdes et al. 2014).

A recent review by Jeremy Reiter, one of the world's leading figures in the primary cilium field, highlights the most relevant known pathways in the primary cilium, being of special importance the GPCR signaling. Furthermore, it points to the need of further research on the physiology of tyrosine kinase receptors in the primary cilium (Hilgendorf et al. 2024). Based on our results and the papers discussed (Yeh et al. 2013; Gerdes et al. 2014), we propose that a putative subpopulation of ciliary IR maybe related to insulin paracrine actions on alpha-cell function. Whether ciliary IRs are present in alpha-cells, and whether their signalling pathways are canonical remain to be elucidated and it will be part of our next research project. These studies will potentially be challenging, since reliable antibodies for IR immunostaining are not available, and IR-Tag overexpression may lead to artefactual IR localization. Further work is needed to study the relevant ciliary signals that control glucagon secretion, including not only insulin signalling but those involving GPCRs, such as somatostatin, glucagon and epinephrine.

On the other hand, our results clearly and unquestionably show that physiological glucagon secretion requires a complete primary cilium. This is because four models of impaired ciliogenesis (A-IDE-KO islets, IDE-KD alpha-cells, ARL13B-KD alpha-cells and IFT88-KD alpha-cells) show dysregulated glucagon secretion.

Unexpectedly, we observed a discrepancy in glucagon secretion responses between the A-IDE-KO islets previously published (Merino et al. 2022) and IDE-KD alpha-cell line in this manuscript, despite both models exhibiting impaired glucose sensing in alpha-cells. A-IDE-KO islets secrete normal levels of glucagon at low glucose levels, but do not display inhibition of glucagon release at high glucose levels. In a different way, IDE-KD alpha-cells show similar glucagon secretion level at low and high glucose; lacking low-glucose glucagon secretion stimulation. Our results using the A-IDE-HT islets (with partial loss of IDE as in the IDE-KD cells) point to the fact that alpha-cells in A-IDE-KO and AÍDE-HT islets receive paracrine inputs from neighbouring beta- and delta-cells, whereas the IDE-KD model only contains alpha-cells, emphasizing the relevance of paracrine signals in the regulation of glucagon secretion.

These results helped us to understand the physiological role of IDE-primary cilium axis in glucagon secretion. IDE acts as a glucose-sensor as demonstrated by the decreased IDE levels during the inhibitory phase of glucagon secretion (16mM glucose). This reduction leads to diminished levels of tubulin, cilium markers (ARL13B

and acetylated tubulin), as well as insulin receptor levels. We interpret these findings as indicating that IDE is able to sense different glucose concentrations. This idea aligns with previous publications that have pointed to the regulation of IDE action by ATP (Song et al. 2004). Glucose sensing by IDE would lead to post-translational changes in tubulin (i.e., tubulin acetylation) which in turn, regulates microtubule dynamics and is required for cilium axoneme formation (Janke and Bulinski 2011; Gadadhar et al. 2017). Microtubule dynamics (polymerization and depolymerization) have been reported to be part of the exocytic machinery of secretory cells (Severin et al. 1991; Ho et al. 2020). Thus, tubulin post-translational modifications may be required for microtubule dynamics and exocytosis. On the other hand, impairment of the primary cilium would affect the presence of the ciliary IR, which is diminished at high glucose concentrations.

From a physiological point of view, it is interesting to observe how, the alpha-cell reduces IRs when glucose concentrations are high and insulin levels are increased, in order to avoid excessive insulin signals.

The major limitation of our study is that, to definitively demonstrate the effect of IDE on glucagon secretion through the tubulin-primary cilium axis, we would need to conduct rescue experiments. Normalised glucagon secretion in IDE-KD cells with a restored primary cilium would confirm the existence of a tubulin-primary cilium axis downstream of IDE.

Conclusions

In conclusion, our results reveal a previously unknown mechanism of glucose sensing to control glucagon secretion, which involves IDE, tubulin cytoskeleton and the primary cilium. This mechanism is likely to be mediated by tubulin post-translational modifications as acetylation. These findings identify molecular targets for potential drugs to correct glucagon secretion in diabetes.

Abbreviations

A-IDE-KO	Alpha-cell specific IDE knock-out mouse
A-IDE-HT	Alpha-cell specific IDE heterozygous mouse
B-IDE-KO	Beta-cell specific IDE knock-out mouse
IDE	Insulin-degrading enzyme
IFT88	Intraflagelar transport protein 88
IP	Immunoprecipitation
IR	Insulin receptor
KATP channel	ATP-sensitive potassium channel
STORM	Stochastic Optical Reconstruction Microscopy
T2D	Type 2 diabetes

Supplementary Information

The online version contains supplementary material available at https://doi.org/10.1186/s10020-026-01428-1.

Supplementary Material 1: Supplementary Fig. 1. Si-scramble cells behave as no-siRNA treated cells. To determine whether siRNA mediated knock-down in the three models differ from no-siRNA treated alpha-cells, we performed RT-PCRs comparing αTC1.9 cells without siRNA (no-siRNA) with the following siRNA-transfected cells: (A) siRNA-IDE, (B) siRNA-ARL13B, and (C) siRNA-IFT88. $N=6$. No differences were observed.

Supplementary Material 2: Supplementary Fig. 2. Inhibition of Dync1h1 expression by SiRNA doesn´t affect glucagon secretion. A. Quantification of Dync1h1 gene expression by RT-PCR, $N=6$. B. Representative western-blot analysis of Dync after 48 h of siRNA-Dync1h1 (Dync-KD) and siRNA-scramble (control) transfection. C. Quantification of Dync/GAPDH in IDE-KD and control cells, $N=9$. D. Glucagon secretion after Dync inhibition, $N=9$. $^{*}p<0.05$, $^{**}p<0.01$, $^{****}p<0.0001$. Data are represented as mean ± SEM.

Supplementary Material 3: Supplementary Fig. 3. Dot plot showing enrichment in cellular processes GO terms for DE genes. Enrichment scores (adjusted p-values) are represented by color gradient. Dot size represents the gene count (number of DE genes). Horizontal axis represents the ratio of the gene count to the total number of annotated genes.

Supplementary Material 4: Supplementary Fig. 4. IDE knock-down by lentiviral ShRNA inhibits glucagon secretion. A. Representative western-blot of IDE in shRNA-control and shRNA-IDE transduced alpha-cells. B. Quantification of IDE western-blot ($N=6$). C. Quantification of *Ide* gene expression by RT-PCR, $N=3$. D. Glucagon secretion in low and high glucose conditions, $N=4$. $^{**}p<0.01$, $^{***}p<0.001$. Data are represented as mean ± SEM.

Supplementary Material 5: Supplementary Fig. 5. impaired glucagon and insulin secretion in A-IDE-HT alpha-cells. A. Low glucose (1mM) stimulates glucagon secretion in A-IDE-WT alpha-cells and high glucose (16mM) inhibits it, meanwhile, A-IDE-HT alpha-cells have lost glucagon secretion inhibition at high glucose, $N=12$. B. A-IDE-WT alpha-cells inhibit glucagon secretion in presence of insulin, but A-IDE-HT alpha-cells have lost insulin inhibitory capacity, $N=12$. C. Constitutive insulin secretion in islets of A-IDE-HT mice (it was measured in the same samples that A) $^{*}p<0.05$. Data are represented as mean ± SEM.

Supplementary Material 6.

Acknowledgements

We thank Biostatista (https://biostatista.com) for assistance with microarray data analyses. We acknowledge support from the Scientific Network Conexión Enfermedades Metabólicas (COMETA) funded by the Consejo Superior de Investigaciones Científicas (CSIC), Spain.

Authors' contributions

Conceptualization: GP and IC; Methodology: PC, MAR, EC, AS, SE, MCD, CR, PP, TR, BM, IC; Validation: PC, MAR, EC, AS, AV, SE, MCD, CR, PP, TR, BM, IC; Formal Analysis: CR, BM, GP and IC; Investigation: PC, MAR, EC, AS, AV, SE, MCD, CR, PP, TR, BM, IC; Resources: GP and IC; Writing - Original Draft: GP and IC; Writing - Review & Editing: PC, MAR, EC, AS, AV, SE, MCD, CR, PP, TR, BM, GP, IC; Visualization: EC, AS, AV, GP, IC; Supervision: BM, GP and IC; Funding Acquisition: BM, GP and IC. All authors have read and agreed to the published version of the manuscript.

Funding

This work was supported by grants PID2019-110496RB-C21 and PID2022-136605OB-C21 to IC; PID2019-110496RB-C22 and PID2022-136605OB-C22 to GP; PID2021-128264OB-I00 and CNS2023-143960 to CMR funded by MICIU/AEI/https://doi.org/10.13039/501100011033 "ERDF A way of making Europe"; Grant VA129P24 to BM and IC funded by Junta de Castilla y León and the European Social Fund (ORDER EDU/841/2024); BT1D (former JDFRF) Career Development Award (5-CDA-2020-949-A-N) to TR. EC and AS were supported by fellowships from the Junta de Castilla y León and the European Social Fund. AV was supported by postdoctoral contract from the Junta de Castilla y León and the European Social Fund (ORDER EDU/841/2024).

Data availability

The data generated and analyzed during the proteomic study are available in the article and in its online supplementary material. In addition, mass spectrometry proteomics data have been deposited to the ProteomeXchange Consortium via the PRIDE partner repository (Perez-Riverol, et al. 2019), Accession Number: PXD065342 (token for reviewer: HS7BSCXoCM4j). The datasets generated and analyzed during the transcriptomic study are available in the GEOarchive repository, Accession Number: GSE297590 (token for reviewer: obgxmouoxbeztkf).

Declarations

Ethics approval and consent to participate
Studies involving animals: A-IDE-KO mice (Gcg-CreERT2; Idef/f) and their controls were generated at the University of Valladolid (UVa) Animal Facility. The Animal Care and Use Committee of the UVa approved all experiments (protocol #8608731). All experiments were performed in accordance with EU guidelines and regulations. Authors complied with the ARRIVE guidelines.

Competing interests
The authors declare no competing interests.

Author details
[1]Institute of Biomedicine and Molecular Genetics (Consejo Superior de Investigaciones Científicas-Universidad de Valladolid), Valladolid, Spain
[2]Instituto Biosanitario de Valladolid (IBiOVALL), Valladolid, Spain
[3]IGF, Univ Montpellier, CNRS, Inserm, Montpellier, France
[4]Biomedicine, Biotechnology and Public Health Department, Cádiz University, Cádiz, Spain
[5]Biomedical Research and Innovation Institute of Cadiz (INiBICA), Cadiz, Spain
[6]IMDEA Research Institute of Food & Health Sciences, Madrid, Spain
[7]Institute of Diabetes Research, Helmholtz Zentrum München, German Research Center for Environmental Health, Munich-Neuherberg, Germany
[8]German Center for Diabetes Research (DZD), Neuherberg, Germany
[9]Departamento de Biología Celular, Genética, Histología y Farmacología, Facultad de Medicina, Universidad de Valladolid, Valladolid, Spain
[10]Centro de Investigación Biomédica en Red de Diabetes y Enfermedades Metabólicas Asociadas (CIBERDEM), Madrid, Spain

Received: 5 January 2026 / Accepted: 26 January 2026
Published online: 10 February 2026

References

Alexa A, Rahnenfuhrer J, Lengauer T. Improved scoring of functional groups from gene expression data by decorrelating GO graph structure. Bioinformatics. 2006;22:1600–7.
Arenas-De Larriva MDS, Fernandez-Vega A, Jurado-Gamez B, Ortea I. DiaPASEF proteomics and feature selection for the description of sputum proteome profiles in a cohort of different subtypes of lung cancer patients and controls. Int J Mol Sci. 2022;23:8737.
Carvalho BS, Irizarry RA. A framework for oligonucleotide microarray preprocessing. Bioinformatics. 2010;26:2363–7.
Cho JH, Hughes JW. Cilia action in islets: lessons from mouse models. Front Endocrinol (Lausanne). 2022;13:922983.
Cho JH, et al. Islet primary cilia motility controls insulin secretion. Sci Adv. 2022;8:eabq8486.
Christensen ST, Morthorst SK, Mogensen JB, Pedersen LB. Primary cilia and coordination of receptor tyrosine kinase (RTK) and transforming growth factor beta (TGF-beta) signaling. Cold Spring Harb Perspect Biol. 2017;9:a028167.
Demichev V, Messner CB, Vernardis SI, Lilley KS, Ralser M. DIA-NN: neural networks and interference correction enable deep proteome coverage in high throughput. Nat Methods. 2020;17:41–4.
Edwards JD. Practical application of oxygen transport principles. Crit Care Med. 1990;18:S45–48.
Eschbach J, et al. Dynein mutations associated with hereditary motor neuropathies impair mitochondrial morphology and function with age. Neurobiol Dis. 2013;58:220–30.
Fernandez-Diaz CM, et al. Insulin degrading enzyme is up-regulated in pancreatic beta cells by insulin treatment. Histol Histopathol. 2018;33:1167–80.
Fernandez-Diaz CM, et al. Pancreatic beta-cell-specific deletion of insulin-degrading enzyme leads to dysregulated insulin secretion and beta-cell functional immaturity. Am J Physiol Endocrinol Metab. 2019;317:E805–19.
Gadadhar S, Bodakuntla S, Natarajan K, Janke C. The tubulin code at a glance. J Cell Sci. 2017;130:1347–53.
Gao R, Acreman S, Ma J, Abdulkader F, Wendt A, Zhang Q. alpha-cell electrophysiology and the regulation of glucagon secretion. J Endocrinol. 2023;258:e220295.
Gerdes JM, et al. Ciliary dysfunction impairs beta-cell insulin secretion and promotes development of type 2 diabetes in rodents. Nat Commun. 2014;5:5308.
Gilon P. The role of alpha-Cells in islet function and glucose homeostasis in health and type 2 diabetes. J Mol Biol. 2020;432:1367–94.
Girard D, Petrovsky N. Alstrom syndrome: insights into the pathogenesis of metabolic disorders. Nat Rev Endocrinol. 2011;7:77–88.
Hao K, Chen Y, Yan X, Zhu X. Cilia locally synthesize proteins to sustain their ultrastructure and functions. Nat Commun. 2021;12:6971.
Hartig SM, Cox AR. Paracrine signaling in islet function and survival. J Mol Med (Berl). 2020;98:451–67.
Hilgendorf KI, Myers BR, Reiter JF. Emerging mechanistic Understanding of cilia function in cellular signalling. Nat Rev Mol Cell Biol. 2024;25:555–73.
Ho KH, et al. Glucose regulates microtubule disassembly and the dose of insulin secretion via Tau phosphorylation. Diabetes. 2020;69:1936–47.
Hughes JW, et al. Primary cilia control glucose homeostasis via islet paracrine interactions. Proc Natl Acad Sci U S A. 2020;117:8912–23.
Iliuta IA, et al. Shared pathobiology identifies AMPK as a therapeutic target for obesity and autosomal dominant polycystic kidney disease. Front Mol Biosci. 2022;9:962933.
Janke C, Bulinski JC. Post-translational regulation of the microtubule cytoskeleton: mechanisms and functions. Nat Rev Mol Cell Biol. 2011;12:773–86.
Kawamori D, et al. Insulin signaling in alpha cells modulates glucagon secretion in vivo. Cell Metab. 2009;9:350–61.
Khan AO, et al. Post-translational polymodification of beta1-tubulin regulates motor protein localisation in platelet production and function. Haematologica. 2022;107:243–59.
Lee EY, Hughes JW. Rediscovering primary cilia in pancreatic Islets. Diabetes Metab J. 2023;47:454–69.
Merino B, et al. Insulin-degrading enzyme ablation in mouse pancreatic alpha cells triggers cell proliferation, hyperplasia and glucagon secretion dysregulation. Diabetologia. 2022;65:1375–89.
Muller A, et al. Structure, interaction and nervous connectivity of beta cell primary cilia. Nat Commun. 2024;15:9168.
Pablos M, Casanueva-Alvarez E, Gonzalez-Casimiro CM, Merino B, Perdomo G, Cozar-Castellano I. Primary cilia in pancreatic beta- and alpha-Cells: time to revisit the role of Insulin-Degrading enzyme. Front Endocrinol (Lausanne). 2022;13:922825.
Perez-Riverol Y, et al. The PRIDE database and related tools and resources in 2019: improving support for quantification data. Nucleic Acids Res. 2019;47:D442–50.
Ritchie ME, et al. Limma powers differential expression analyses for RNA-sequencing and microarray studies. Nucleic Acids Res. 2015;43:e47.
Rojas-Torres M, et al. Unraveling the differential mechanisms of revascularization promoted by MSCs & ECFCs from adipose tissue or umbilical cord in a murine model of critical limb-threatening ischemia. J Biomed Sci. 2024;31:71.
Sakamoto K, et al. Loss of Dnah5 Downregulates Dync1h1 Expression, Causing Cortical Development Disorders and Congenital Hydrocephalus. Cells. 2024;13.
Sanchez GM, et al. The beta-cell primary cilium is an autonomous Ca2 + compartment for paracrine GABA signaling. J Cell Biol. 2023;222:e202108101 .
Severin FF, Shanina NA, Kuznetsov SA, Gelfand VI. MAP2-mediated binding of chromaffin granules to microtubules. FEBS Lett. 1991;282:65–8.
Sewell MT, Legue E, Liem KF Jr. Tubb4b is required for multi-ciliogenesis in the mouse. Development. 2024;151:dev201819.
Shankar S, et al. Alpha gamma-tubulin complex-dependent pathway suppresses ciliogenesis by promoting cilia disassembly. Cell Rep. 2022;41:111642.
Song ES, Juliano MA, Juliano L, Fried MG, Wagner SL, Hersh LB. ATP effects on insulin-degrading enzyme are mediated primarily through its triphosphate moiety. J Biol Chem. 2004;279:54216–20.
Tyanova S, et al. The perseus computational platform for comprehensive analysis of (prote)omics data. Nat Methods. 2016;13:731–40.
Volta F, et al. Glucose homeostasis is regulated by pancreatic beta-cell cilia via endosomal EphA-processing. Nat Commun. 2019;10:5686.
Wendt A, Eliasson L. Pancreatic alpha-cells - The unsung heroes in islet function. Semin Cell Dev Biol. 2020;103:41–50.
Xu E, et al. Intra-islet insulin suppresses glucagon release via GABA-GABAA receptor system. Cell Metab. 2006;3:47–58.
Yeh C, Li A, Chuang JZ, Saito M, Caceres A, Sung CH. IGF-1 activates a cilium-localized noncanonical Gbetagamma signaling pathway that regulates cell-cycle progression. Dev Cell. 2013;26:358–68.

Zaghloul NA, Katsanis N. Mechanistic insights into Bardet-Biedl syndrome, a model ciliopathy. J Clin Invest. 2009;119:428–37.
Zhou X, Cao J, Xie J, Tong W, Jia B, Fu J. Effect of Dync1h1 on phototransduction protein transport and the development and maintenance of photoreceptor cells in zebrafish. Invest Ophthalmol Vis Sci. 2025;66:38.

Publisher's note